Parameter estimation for heavy binary-black holes with networks of second-generation gravitational-wave detectors

Salvatore Vitale,[1,*] Ryan Lynch,[1] Vivien Raymond,[2] Riccardo Sturani,[3] John Veitch,[4] and Philip Graff[5]

[1]*LIGO, Massachusetts Institute of Technology, Cambridge, Massachusetts 02139, USA*
[2]*Albert-Einstein-Institut, Max-Planck-Institut fur Gravitationsphysik, D-14476 Potsdam-Golm, Germany*
[3]*International Institute of Physics (IIP), Universidade Federal do Rio Grande do Norte (UFRN) CP 1613, 59078-970 Natal-RN, Brazil*
[4]*School of Physics and Astronomy, University of Birmingham, Birmingham, B15 2TT, United Kingdom*
[5]*Department of Physics & Joint Space-Science Institute, University of Maryland, College Park, Maryland 20742, USA*

(Received 15 November 2016; published 28 March 2017)

The era of gravitational-wave astronomy started with the discovery of the binary black hole coalescences (BBH) GW150914 and GW151226 by the LIGO instruments. These systems allowed for the first direct measurement of masses and spins of black holes. The component masses in each of the systems have been estimated with uncertainties of over 10%, with only weak constraints on the spin magnitude and orientation. In this paper we show how these uncertainties are typical for this type of source when using advanced detectors. Focusing, in particular, on heavy BBH of masses similar to GW150914, we find that typical uncertainties in the estimation of the source-frame component masses will be around 40%. We also find that for most events the magnitude of the component spins will be estimated poorly: for only 10% of the systems, the uncertainties in the spin magnitude of the primary (secondary) BH will be below 0.7 (0.8). Conversely, the effective inspiral spin along the angular momentum can be estimated more precisely than either spins, with uncertainties below 0.16 for 10% of the systems. We also quantify how often large or negligible primary spins can be excluded and how often the sign of the effective spin can be measured. We show how the angle between the spin and the orbital angular momentum can only seldom be measured with uncertainties below 60°. We then investigate how the measurement of spin parameters depends on the inclination angle and the total mass of the source. We find that when precession is present, uncertainties are smaller for systems observed close to edge-on. Contrarily to what happens for low-mass, inspiral-dominated sources, for heavy BBH we find that large spins aligned with the orbital angular momentum can be measured with a small uncertainty. We also show how spin uncertainties increase with the total mass. Finally, considering a simple toy model, we show how detections can be combined to infer properties of the underlying population.

DOI: 10.1103/PhysRevD.95.064053

I. INTRODUCTION

The Advanced LIGO [1] observatories discovered gravitational waves (GWs) emitted by a binary black hole coalescence (BBH) on September 14, 2015 [2]. The event was named GW150914. A few months later, a second clear BBH detection (GW151226) was made [3,4], and a weaker candidate BBH signal (LVT151012) was also identified.

The key astrophysical parameters of these sources have been estimated using Bayesian algorithms [3–7], and tests of general relativity have been performed [4,8,9]. The source-frame masses of the two black holes in GW150914 have been estimated [4,6] to be $36.2^{+5.2}_{-3.8}\ M_\odot$ and $29.1^{+3.7}_{-4.4}\ M_\odot$, where the error bars include both statistical and systematic errors from waveform mismatch, with the statistical uncertainty contributing the most. For GW151226 the two masses have been estimated with similar large uncertainties to be $14.2^{+8.3}_{-3.7}\ M_\odot$ and $7.5^{+2.3}_{-2.3}\ M_\odot$ [4].

Within general relativity, the dimensionless spin magnitude can take values in the range [0, 1], with 0 being nonspinning and 1 being maximally spinning. For both sources, the spins of the two black holes have been measured with high uncertainty, the 90% credible interval on the measurement spanning most of the prior support. For GW150914, the median and 90% credible interval were $0.32^{+0.47}_{-0.29}$ and $0.48^{+0.47}_{-0.43}$ [6]. Something more could be said about the spins of GW151226, for which there was evidence that at least one of the spins was larger than zero [3,4], but no meaningful constraint on the spin tilt angles has been set for any of the systems.

Precise estimation of masses and spins of black holes from gravitational-wave sources will contribute toward the understanding of the formation and the properties of these objects, and will complement measurements made with electromagnetic radiation. For example, both masses and

*salvatore.vitale@ligo.org

spins of black holes can be measured for black holes in x-ray binaries, but those are indirect measurements. The mass is found by measuring the mass of the companion object and the projection of the radial velocity along the line of sight (which is degenerate with the inclination of the orbital plane) [10]. The masses of several black holes have been estimated using this method, with values that cover the range $[5–15]\ M_\odot$ [11]. Two main methods exist to measure spins [12–15], both of which rely on modeling the disk surrounding the BH. The mass and spin estimation of GW150914 and GW151226 thus represent the first direct measurements of such quantities.

The main astrophysical implications of the discoveries have been discussed in [4,16], while a prediction of the rate of heavy BBH coalescence and prospects for detection in future observing runs was given in [17] (and later updated in [4]). The rate estimates suggest that the number of significant BBH detections by ground-based detectors could already be around one per month in the second observing run, starting before the end of 2016 [18]. In view of the numerous detections that will be made in the next few years, it is worth addressing the following question: was the precision in the measurement of parameters for the detected systems typical of what we can expect in the future? In this paper we address that question. Since results already exist in the literature (see below) for lighter BBH, here we thus focus on heavy BBH. These are systems that will only be in band for a few cycles before merger, thus making unclear, *a priori*, what and to which precision can be deduced about the individual binary constituent parameters. Furthermore, given that advanced detectors have a selection bias toward higher masses [19], one might expect heavy BBH to be detected more often, if the rates are comparable to those for stellar-mass BBHs.

Some previous studies of parameter estimation for BBH (including heavy BBH) have been performed. Reference [20] considers BBHs with spins aligned with the orbital angular momentum (i.e., without spin-induced precession) and reports statistical uncertainties for the main astrophysical parameters. Its results are comparable to ours for BBH of similar mass, although the reported uncertainties are slightly smaller since they do not have potential correlations coming from the precessing spin degrees of freedom. More recently, Ref. [21] considered neutron star–black hole systems. Their uncertainties in the spin parameters are smaller than what we find here, consistently with the fact that larger mass ratios enhance the measurability of spins [22]. Most of the early work, e.g., Refs. [23,24], deals with only a few systems at a time, using post-Newtonian inspiral-only waveforms. As such, these papers are not directly comparable to ours.

We create an astrophysical population of 200 spinning heavy BBHs and estimate their parameters with a network of advanced LIGO and Virgo detectors at design sensitivity. We find that source-frame component masses can be estimated with typical uncertainties of 40%. This is slightly larger than what was measured for GW150914, owing to its large signal-to-noise ratio. Spin magnitude is hard to estimate: for the most (least) massive black hole in the system, we find that only 10% of the time will the 90% credible interval uncertainty be smaller than 0.7 (0.8). Similar conclusions hold for the tilt angles, i.e., the angle between each spin vector and the orbital angular momentum, for which the uncertainties will be larger than 60° for most systems. As we mentioned above, GW150914 fits perfectly in this scenario. We quantify how often large and negligible spins can be excluded, and we find that large spins are easier to exclude. For example, if only BBH with primary spins up to 0.2 are considered, 90% of the time spins above 0.95 can be excluded. We also very that effective inspiral spin (henceforth, simply effective spin) along the orbital angular momentum [4,6] can be estimated more precisely than the individual spins, and that 70% of the times one can correctly measure the sign of the effective spins, if the underlying population has even mild effective spins (below -0.3 or above 0.3).

We then show how precessing spins can be estimated more precisely as the orbital inclination angle moves away from zero, and the uncertainties reach a minimum for angles close to $\pi/2$, where the binary is viewed in alignment with the orbital plane. Contrarily to what is expected for low-mass sources, dominated by the inspiral phase, we find that heavy BBH spins aligned with the orbital angular momentum are not extremely degenerate with the mass parameters and can thus be measured very precisely. In fact, considering BBH with mass ratios of 1 and 2 and spin magnitude of 0.9, we find that aligned spins can be measured by a factor of several better than precessing spins, no matter what the orbital orientation is.

We investigate how the uncertainties depend on the (redshifted) total mass of the system and find that the uncertainties increase with the total mass, with larger increases for larger mass ratios.

Finally, we show how the properties of the underlying astrophysical distribution can be estimated, in a very simple toy model.

The rest of this paper is organized as follows. We first describe the GW network (Sec. II A) and BBH events (Sec. II B) used in this study. The main results are summarized in Sec. III, while conclusions and a discussion can be found in Sec. VI.

II. METHOD

A. Detectors

In this study, we consider a network of three advanced detectors—the two LIGO interferometers (IFOs) and the Virgo detector, HLV network. (In the Appendix we will consider a five-detector network that includes the three instruments above plus the KAGRA detector in Japan [25] and LIGO India [26], HVLIJ network.) For all instruments,

we used the noise spectral density corresponding to their design sensitivities [1,27]. We are thus focusing on instruments that will be available later in the decade. However, it is easy to realize that the main results we obtain will not strongly depend on this choice. The main difference in the detected events if the instruments are made more sensitive is that the distance distribution of the detected events will get shifted to higher values while keeping roughly the same shape.[1] Critically, the distribution of the signal-to-noise ratios (SNRs) will be the same. Since the uncertainty in the intrinsic parameters (mass, spins) mostly depends on the SNR, with the caveat above,[1] the distribution of uncertainties we obtain should be representative of the uncertainties of the next few years. In fact, we will see that the uncertainties of GW150914 follow very well the ones we obtain here.

B. Simulated events

We simulated 200 binary black hole systems with intrinsic masses uniformly drawn from the range [30–50] $M_\odot$, and dimensionless spin magnitudes $a \equiv \frac{c|\vec{S}|}{Gm^2}$ drawn uniformly from the range [0, 0.98]. The sky position and orientation of the systems are isotropically distributed. The distances are drawn uniformly in comoving volume, with a lower network signal-to-noise ratio (that is, the quadrature sum of the SNR in each instrument) cut at 12. This corresponds to distances up to ∼12 Gpc, or a redshift of ∼1.5 using a ΛCDM flat cosmology [30]. The redshift distribution of the simulated signals is shown in Fig. 1, with a vertical line showing the median measured redshift of GW150914.

We notice that GW150914 is on the left side of the distribution since it was detected by two LIGO instruments at early sensitivity [6,31], while in this paper we consider a network made of more sensitive detectors.

In Fig. 2 we show the network SNR of the population of BBH. Here, too, a vertical dashed line shows the SNR of GW150914. We see that, even when considering a three-detector network at design sensitivity, as we do in this work, GW150914 is considerably louder than the "typical" detection.

The simulations were performed using the IMRPhenomPv2 waveform approximant [32–34]. This is a phenomenological inspiral-merger-ringdown approximant, and it is one of the two used to estimate the parameters of the detected events [3,4,6]. It must be stressed that IMRPhenomPv2 uses a simplified spin description [32,35], in which the main spin parameters are the effective components of the total spins along the orbital angular momentum ($\chi_{\rm eff}$ in [6]) and perpendicular to it (χ_p in [6]). The magnitude and orientations of the component spins

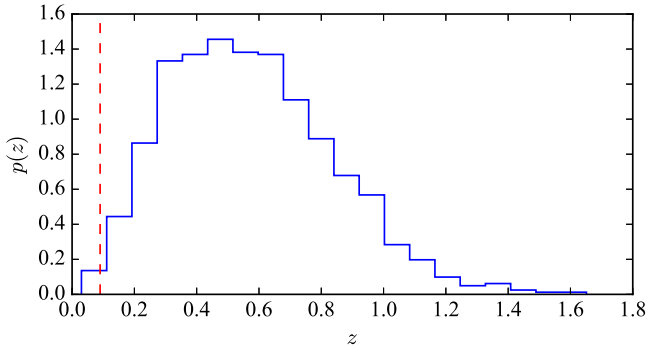

FIG. 1. The redshift distribution of detectable heavy BBH with a network of LIGO and Virgo at design sensitivity. The vertical dashed line is the median estimated redshift for GW150914 [4].

can be obtained from those. Although IMRPhenomPv2 uses a simplified spin prescription, it has been shown for GW150914 that the results obtained with IMRPhenomPv2 broadly agree with those obtained with a fully precessing time-domain approximant (SEOBNRv3) [7]. The agreement might be inferior in some corners of the parameter space (e.g., for systems seen from edge-on, i.e., with their orbital angular momentum forming an angle of $\iota \sim \pi/2$ with the line of sight) [36]. However, IMRPhenomPv2 is more than 1 order of magnitude faster to compute than SEOBNRv3 for the masses considered in this study. Considering that a single parameter estimation run requires the computation of $\sim 10^6$ waveforms, we will thus work with the former. When surrogate reduced order models (ROMs) [37–40] become available for SEOBNRv3, possibly followed-up by reduced order quadrature [41,42], this study should be repeated. However, the main conclusions of this study should hold since most events detected by advanced detectors will be oriented close to face-on ($\iota \sim 0$) or face-off ($\iota \sim \pi$) [43].

By using the same waveform family to simulate the signals and to estimate their parameters, we do not consider any effect of waveform systematics. In practice, different waveform families will always lead to slightly different

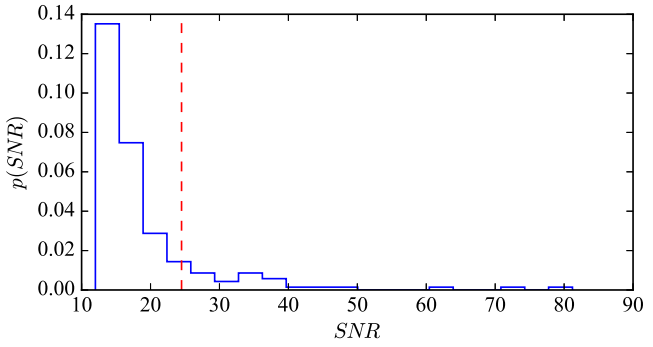

FIG. 2. The SNR distribution of detectable heavy BBH with a network of LIGO and Virgo at design sensitivity. The vertical dashed line is the SNR of GW150914 [4].

[1]This would not be true if the increase in sensitivity is such that sources at redshifts of several are reached [28,29]; however, this will not be the case for systems in the mass range we consider.

parameter estimates, but here we assume that those differences will keep becoming smaller in the next months and years, as more and more elaborate waveform families are introduced.

All simulated BBH are added ("injected") into simulated interferometric data of advanced LIGO and Virgo.

Algorithms to estimate parameters of spinning compact binary coalescence (CBC) signals have been developed over the last several years, based on either Monte Carlo [24,44] or nested sampling [45] methods. In this paper we use the algorithm that yielded estimates for the two detected events [4], `lalinference` [5].

III. RESULTS

In what follows we will use the symbol Σ_x to refer to the 90% credible interval (CI) for the parameter x (with dimensions), and the symbol Γ_x for the relative uncertainty w.r.t. the true value: $\Gamma_x \equiv \Sigma_x / x_{\rm true}$ (dimensionless). Our Σ will thus be directly comparable with the uncertainties as reported for GW150914 and GW151226.

A. Masses

We start by looking at the estimation of mass parameters. When sources at non-negligible redshifts are being detected, one must distinguish between the intrinsic (or source-frame) masses and the detector-frame (or redshifted) masses. Using an index s for source-frame quantities and an index d for detector-frame quantities, the relationship is trivially

$$m^d = (1+z)m^s, \tag{1}$$

where by m we generically indicate any mass parameter. In what follows we will use m_i for the component masses, M for the total mass and $q = m_2/m_1 \in [0,1]$ for the asymmetric mass ratio. All masses will be expressed in units of solar masses. We will examine both intrinsic and redshifted masses because while intrinsic masses are what is astrophysically relevant, it is the redshifted masses that control the shape and phase evolution of the signals in the instruments and hence impact the uncertainties.

It is known that for low-mass CBC such as binary neutron stars or systems containing stellar-mass BHs, GWs can yield extremely precise measurements of the chirp mass $\mathcal{M} \equiv \frac{(m_1 m_2)^{3/5}}{M^{1/5}}$. On the other hand, uncertainties are larger for the measurement of the component masses, total mass and mass ratio [46–48]. This happens because the chirp mass enters the waveform phase at the lowest order in the inspiral, while the mass ratio (and thus the component masses and total mass) enters at higher orders (see, e.g., Ref. [49]). The situation is different for the heavy BBH we consider in this work since not only the inspiral but also the merger and ringdown phases will be in the bandwidth of the detectors. Since those depend on the *total* mass, we can expect similar uncertainties for the chirp mass and the total mass [50–52]. Furthermore, since the length of the inspiral phase shortens as the mass increases [3,4], the measurement of the chirp mass should slightly worsen as the masses increase.

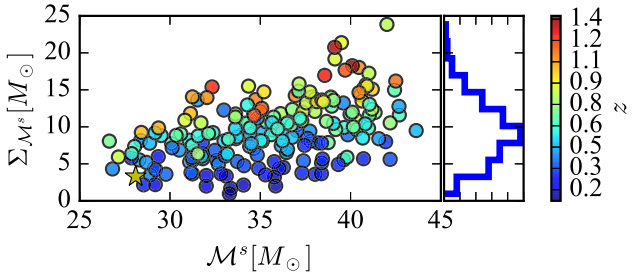

FIG. 3. The distribution of the 90% CI uncertainty in the estimation of the source-frame chirp mass (y axis) against the true source-frame chirp mass (x axis). The color bar is the redshift of the sources. A star reports the coordinates of GW150914.

In Fig. 3 we report the 90% CI for the source-frame chirp mass measurement (y axis) against the true injected source-frame chirp mass, while the color bar reports the injected redshift z. Here and in other plots (unless otherwise indicated) a yellow star reports the values for GW150914 (since we do not know the "true" value in this case, the x axis refers to the median measured values as given in [4]).

We do not see a strong correlation between injected mass and uncertainties. The only clear trend is that closer events have smaller uncertainties, due to their high SNRs. What is happening is that, as mentioned above, the shape of the signal in the detector will depend on the detector-frame masses and thus on the redshift. If one plots the uncertainties against the detector-frame chirp mass, Fig. 4, then the correlation becomes evident.

Typical uncertainties span a broad range, from a few to $\sim$20 $M_\odot$, depending on the detector frame chirp mass. This translates to relative uncertainties (over the injected value) in the range few to 60%, as shown in Fig. 5, where once again the color bar reports the redshift, with a peak at $\sim$30%.

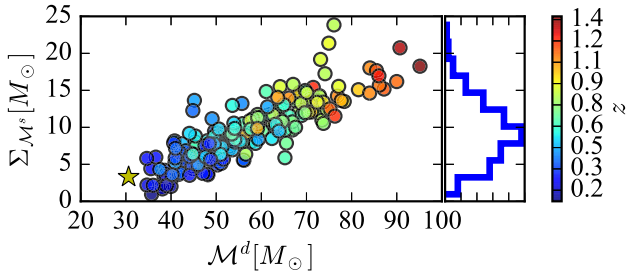

FIG. 4. The distribution of the 90% CI uncertainty in the estimation of the source-frame chirp mass (y axis) against the true detector-frame chirp mass (x axis). The color bar is the redshift of the sources. A star reports the coordinates of GW150914.

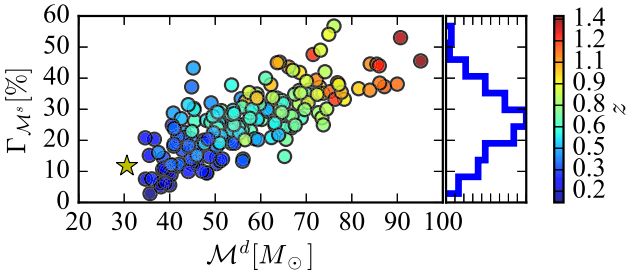

FIG. 5. The distribution of the 90% CI relative uncertainty (in percent over the true value) in the estimation of the source-frame chirp mass (y axis) against the true detector-frame chirp mass (x axis). The color bar is the redshift of the sources. A star reports the coordinates of GW150914.

In all these plots, we see that the uncertainties for GW150914 seem to be quite typical of systems with comparable masses.

From an astrophysical point of view, the most relevant mass parameters are the component masses and, relatedly, the mass ratio. In fact, measuring the masses of heavy BH would allow us to estimate their mass distributions, while the mass ratio can be used to distinguish formation channels [53].

In Fig. 6 we show the relative uncertainties for the source-frame mass of the primary BH (i.e., the most massive) against the intrinsic chirp mass. We see that 90% CI uncertainties of the order of several tens of percent will be common for quiet events, while nearby or loud events can have uncertainties of a few tens of percent. GW150914 lives near the tail of the distribution, with uncertainty of ∼25%, since its SNR is large (∼23.7). The histogram on the right side reports the distribution of the uncertainties. For a population like the one we considered here, the peak is at ∼40%.

A similar plot for the secondary object is shown in Fig. 7. We see that the uncertainties are similar to what was obtained for m_1, with a slightly larger median.

Earlier in this section we mentioned that for heavy BBH, we expect the total mass to be estimated as well as the chirp mass (while for BBH of hundreds of solar masses, it will be estimated better than the chirp mass [50–52]). This is indeed confirmed by Fig. 8, where we see that typical uncertainties in the measurement of the source-frame total mass will be of a few tens of percent, with a peak probability at ∼25%.

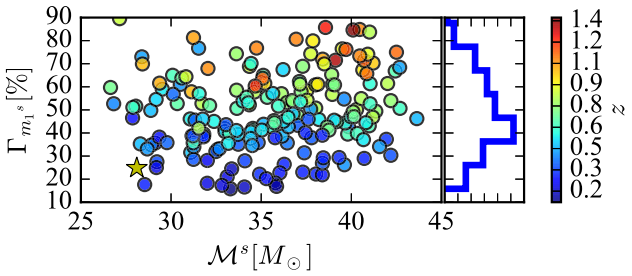

FIG. 6. The distribution of the 90% CI relative uncertainty (in percent over the true value) in the estimation of the source-frame primary mass (y axis) against the true source-frame chirp mass (x axis). The color bar is the redshift of the sources. A star reports the coordinates of GW150914.

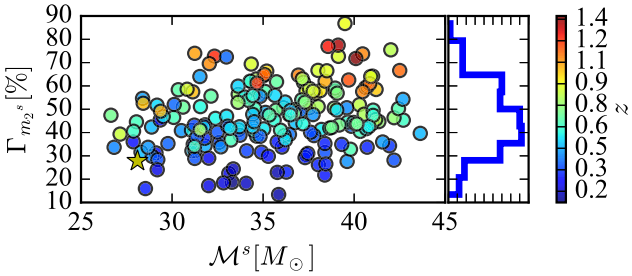

FIG. 7. Like Fig. 6, but for the secondary BH mass. The color bar is the redshift of the sources.

B. Spins

The uncertainties for the spin magnitudes for GW150914 covered most of the prior range, with only extreme spins excluded [4,6]. In [22] we have shown how uncertainties will generally be large for systems with comparable masses, unless the systems are observed from edge-on. However, in that paper we only considered a few corners in the parameter space, and we worked with stellar mass black holes. In this section we show what spin estimation will look like for an astrophysical distribution of more massive BBHs.

In Fig. 9 we show the 90% CI uncertainty in the measurement of the spin magnitude for the most massive BH (y axis) as a function of the redshifted chirp mass. The true spin magnitude is reported in the color bar. The histogram on the right shows the distribution of the uncertainties.

We find that larger spins are often easier to measure, while for small spins the 90% CI does not cover 90% of the prior only occasionally.

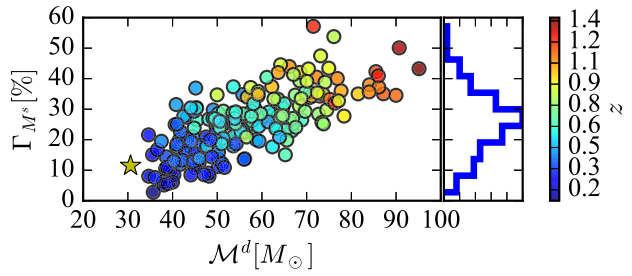

FIG. 8. The distribution of the 90% CI relative uncertainty (in percent over the true value) in the estimation of the source-frame total mass (y axis) against the true detector-frame chirp mass (x axis). The color bar is the redshift of the sources. A star reports the coordinates of GW150914.

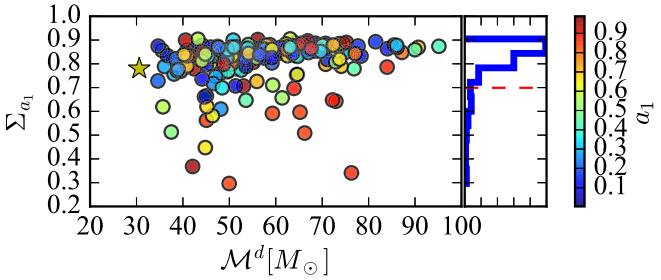

FIG. 9. The distribution of the 90% CI uncertainty in the estimation of the primary spin magnitude (y axis) against the true detector-frame chirp mass (x axis). The color bar shows the magnitude of the primary spin. A star reports the coordinates of GW150914. The dashed line on the histogram marks the abscissa of the 10th percentile.

The dashed red line in the right panel shows the position of the 10th percentile of the uncertainty distribution, at $\Sigma_{a_1} = 0.7$. We thus expect that in only 10% of the cases will we be able to measure the spin magnitude of the primary BH with an uncertainty smaller than 0.7. We do not see a clear correlation of spin uncertainties with the redshifted chirp mass since too many other factors affect the measurability of the spins. Later, in Sec. IV B we will investigate how the spin measurement depends on the mass, working with a controlled setup.

We have indicated with a yellow star the median-recovered spin magnitude and the uncertainty for GW150914, which we see is totally consistent with the uncertainty of the BBH we simulated.

The same type of plot but for the secondary spin is shown in Fig. 10 (note the different range in the y axis). As expected, the uncertainties are much larger for the secondary object (10th percentile at 0.85). We thus conclude that it would be extremely hard to measure the spin magnitude of the secondary object in heavy BBH systems. This conclusion was reached by [54] for spin-aligned BBH, and by [22] for a few precessing stellar mass BBHs.

Two spin values which have special meaning are obviously zero and one, i.e., no spinning and maximally spinning. In fact, one of the main conclusions of the

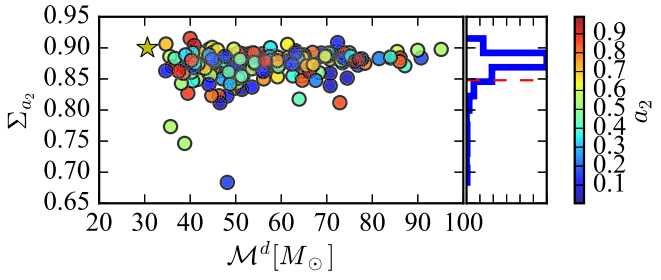

FIG. 10. Same as Fig. 9, but for the secondary spin magnitude. The color bar shows the magnitude of the secondary spin. Note the different range in the y axis.

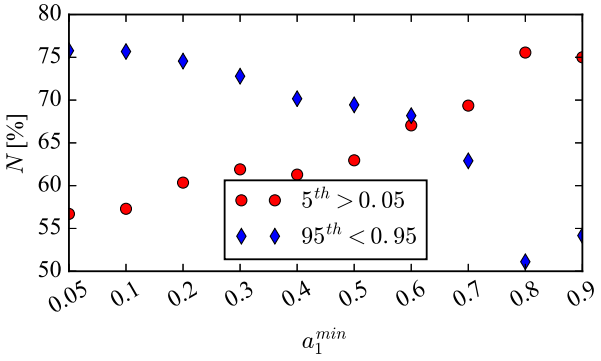

FIG. 11. In the x axis, we give the minimum value of the spin magnitude of the primary BH. The red circles give the fraction of events (y axis) with that minimum spin for which the 5th posterior percentile is larger than 0.05. The blue diamonds report the fraction of events for which the 95th percentile is smaller than 0.95. If the underlying population is made of BH with large spins (right side of the plot) ∼75% of the time, one can exclude that the primary BH had negligible spin.

GW150914 analysis is that the primary BH was not maximally spinning [6], whereas for GW151226, zero spin for at least one of the BHs was excluded with high confidence [3,4].

We have used subsets of our BBH to verify how often we will be able to exclude the extreme scenarios of non-spinning and maximally spinning. We focus on the primary spin since, as we just saw, the secondary one is hardly ever measurable.

Let us first check what conclusions we can draw from subpopulations of BBH with increasingly large primary spins. From our set of BBH, we down-select events with increasingly large minimum values of a_1, from 0.05 to 0.90. We then check for which fraction of them we can

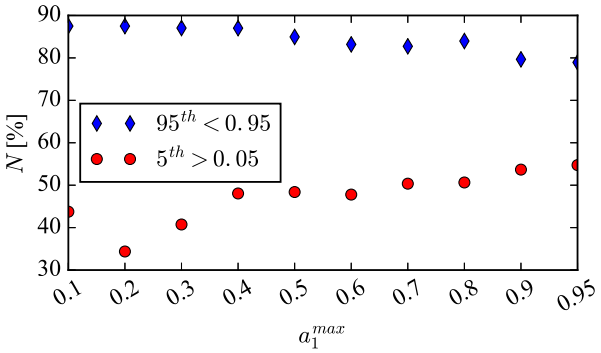

FIG. 12. In the x axis, we give the maximum value of the spin magnitude of the primary BH. The red circles give the fraction of events (y axis) with that maximum spin for which the 5th posterior percentile is larger than 0.05. The blue diamonds report the fraction of events for which the 95th percentile is smaller than 0.95. If the underlying population is made of BH with small spins (left side of the plot) ∼90% of the time, one can exclude that the primary BH had large spin.

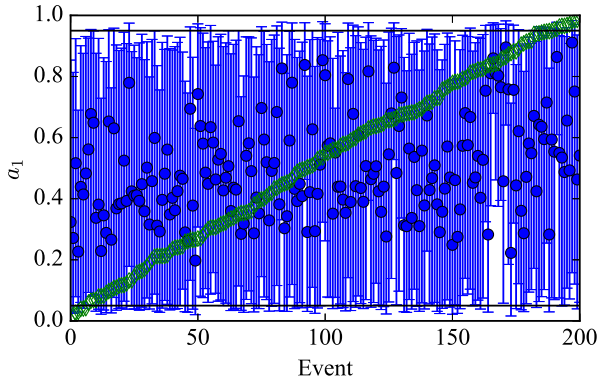

FIG. 13. For all events, median value of the primary BH spin with 90% CI. The empty green diamonds indicate the true spins. The two horizontal black lines are at 0.05 and 0.95.

exclude nonspinning and maximally spinning BHs. This is shown in Fig. 11. The left of the plot, with $a_1^{\min} = 0.05$, thus corresponds to assuming that the astrophysical distribution of a_1 is flat in most of the allowed spin range. At the other extreme, on the right of the plot, one is assuming that nature only produces BHs with large spins in CBCs. Let us first focus on the red circles. They report the fraction of BBH having minimum spin magnitude given in the x axis for which one can conclude $a_1 > 0.05$ at 90% CI. As one would expect, the worst result is obtained when we keep nearly all events ($a_1^{\min} = 0.05$) since that will include events with small spins, for which it will be hard to exclude low spin values (or, actually, to draw any conclusion). As we increase the minimum value of the true spin magnitude, moving to the right of the plot, the fraction of events for which we can exclude small spins increases until it reaches ∼75% when we only keep sources with large spins. We remark that this fraction does not get close to 100%, and even when all systems have large spin on the primary, for ∼20% of them we will not be able to exclude the absence of spin. The blue diamonds in the same plot quantify the fraction of events for which we can exclude that a_1 is larger than 0.95, again at the 90% CI. The curve is roughly a mirror of the previous one. If a whole distribution of spin is considered ($a_1^{\min} = 0.05$), roughly 75% percent of the time, one can exclude very large spins. As the spins increase in the underlying population, the efficiency naturally goes down, until it reaches ∼50%.

One might be surprised that even when the minimum spin is large (say, 0.9) it is still the case that ∼50% of the time the 95th percentile is smaller than 0.95. This happens because, for most events, no matter their spins, the posterior distribution for a_1 will be centered in the middle of the prior, with error bars that cover a large fraction of the prior (see Fig. 13 below and the related discussion).

We next perform the opposite exercise and down-select events with decreasing maximum primary spin, given in the x axis of Fig. 12. Once again, the red circles report the fraction of events for which negligible primary spin can be excluded. We see that this fraction is nearly always below 0.5. Looking at the blue diamonds, i.e., the fraction of events for which nearly maximal spins can be ruled out, we see that this number is close to 90% if only small primary spin systems are used. However, the curve is roughly flat. As we move to large $a_1^{\max}$, we basically consider the whole distribution of spins and obtain the same results of the left side of Fig. 11. It is worth stressing that the efficiency when excluding large spins is nearly always larger than for excluding small spins, the opposite only happening when the spins are in fact large. This is of course yet another way of saying that it is easier to measure large spins than small ones.

Given the relatively high fraction of events for which large spins can be excluded if the underlying population has random spins in the range [0, 1], it is thus not surprising that a similar conclusion could be drawn for GW150914.

In Fig. 13, we explicitly show the 90% CI (as error bars around the median) for all our events, sorted by the true value of the primary spin (empty diamonds). As mentioned above, we see that even for large spins, it is not uncommon that the posterior is centered around medium spins.

Let us now look at the estimation of the effective total spin along the orbital angular momentum. This is a quantity which was referred to as $\chi_{\rm eff}$ in [4,6]. Motivations for the use of this parametrization can be found elsewhere [55–60]. Here we stress that being able to measure the sign of $\chi_{\rm eff}$ with high confidence could help us favor some formation models for compact binaries [61]. In fact, the main claim that could be made about the spins of GW151226 is that $\chi_{\rm eff}$ was positive and nonzero [3,4]. We find that $\chi_{\rm eff}$ is estimated better than either component spins. A similar conclusion was reached by [54] for aligned-spin BBHs. In Fig. 14, we show the distribution of the 90% CI for $\chi_{\rm eff}$ against the detector frame chirp mass. The color bar reports the true $\chi_{\rm eff}$. We see that the uncertainties are typically much smaller than what was obtained while estimating the component spins (Figs. 9 and 10). This is not surprising since it is the total spins, and in particular their projection along the orbital angular momentum, that affect the

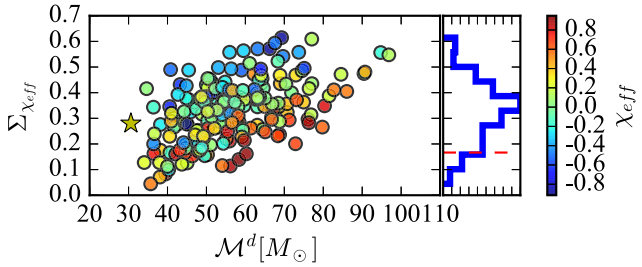

FIG. 14. The distribution of the 90% CI uncertainty in the estimation of $\chi_{\rm eff}$ (y axis) against the true detector-frame chirp mass (x axis). The color bar shows the true $\chi_{\rm eff}$. A star reports the coordinates of GW150914. The dashed line on the histogram marks the abscissa of the 10th percentile.

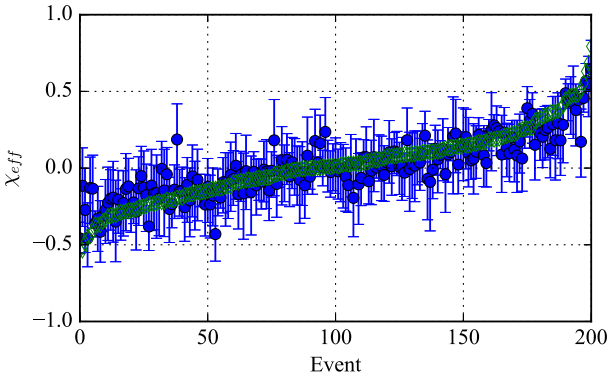

FIG. 15. For all events, with a median value of $\chi_{\rm eff}$ 90% CI. The empty green diamonds indicate the true values.

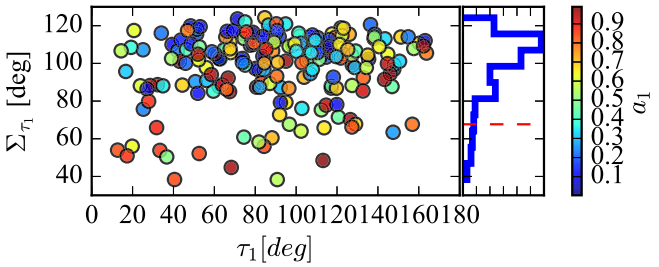

FIG. 17. The distribution of the 90% CI uncertainty in the estimation of the primary spin tilt angle (y axis, degrees) against the true tilt angle (x axis, degrees). The color bar shows the magnitude of the primary spin. The dashed line on the histogram marks the abscissa of the 10th percentile.

waveform length in both the time and frequency domains. In particular, 10% of events will have 90% CI uncertainties below 0.17, with the typical event having uncertainties of ∼0.35. For comparison, GW150914 had a 90% CI of 0.28 [4]. In Fig. 15 we show the median estimates for $\chi_{\rm eff}$ with the 90% CI for all simulated events, with the green diamonds reporting the true simulated values. The small uncertainties suggest one might learn from $\chi_{\rm eff}$ more rapidly than from the component spins. We have verified how often one can exclude negative (positive) values for $\chi_{\rm eff}$ if the underlying population has positive (negative) true values (Fig. 16). The arrows pointing to the left report the fraction of events having $\chi_{\rm eff}$ below the corresponding abscissa for which the 95th percentile of the $\chi_{\rm eff}$ posterior is negative. We see that when the populations has $\chi_{\rm eff}$ below −0.3, ∼70% of events can be correctly identified as having negative $\chi_{\rm eff}$. The leftmost point is not reliable since very few events in our population have $\chi_{\rm eff}$ below −0.4. We expect that if the population extended to more negative values, the efficiency would continue to go up. We see this happening when we perform the opposite exercise (arrows pointing to the right). For example, if the population has positive $\chi_{\rm eff}$ larger than +0.3, 80% of the time negative $\chi_{\rm eff}$ can be excluded. Naturally, the exact numerical values of the efficiency at measuring the sign of $\chi_{\rm eff}$ depend on the population we simulated. However, it seems safe to say that it is a much easier measurement than that of the individual spins.

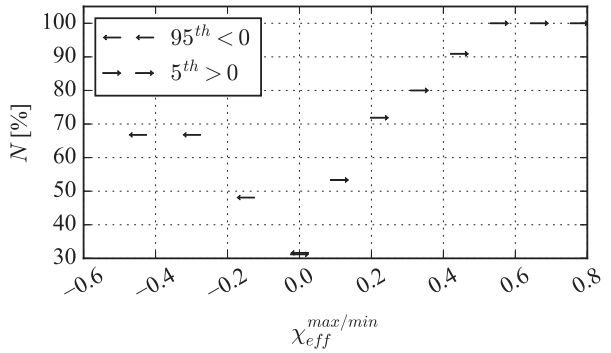

FIG. 16. The arrows pointing to the left report the fraction of events with true $\chi_{\rm eff}$ below that abscissa for which the 95th percentile for $\chi_{\rm eff}$ is below zero. The arrows pointing to the right report the fraction of events with true $\chi_{\rm eff}$ above that abscissa for which the 5th percentile for $\chi_{\rm eff}$ is above zero.

We end this section with a quick discussion of tilt angles, i.e., the angle between the spins and the orbital angular momentum. We focus on the primary object since, as for the spin magnitude, the tilt angle of the secondary object will typically be unmeasurable. The tilt angles are among the key quantities we wish to measure in a BBH since they could directly be linked to the formation channel of CBCs [62–64]. Of course, they are not constant during the evolution of the waveform since both the spins and the angular momentum precess around the total angular momentum. Similarly to what was done in [4,6], we quote the values of tilts at a frequency of 20 Hz.

In Fig. 17 we report the 90% CI for the tilt of the primary, τ_1, against its true value, both in degrees. The spin of the primary is given in the color bar. We see that for the typical event, the uncertainty will be very large: the distribution peaks at ∼110° (histogram on the right panel). Only for ∼6% of the systems will the uncertainty be smaller than 60°. Once again, GW150914 (for which we do not show a star since the medians for the tilt angles were not made public) fits perfectly in this scenario since it was not possible to estimate the orientation for any of the spins [6].

From Fig. 17 we see that large spins are typically required to have a chance of estimating the tilt angle. The other factor that plays a large role in the capability of measuring spin parameters is the orientation of the orbital plane, which we discuss in Sec. IV A.

C. Distance and sky location

We end the analysis of the uncertainties of a population of BBH events with the luminosity distance and sky location. Precise estimation of distance and sky position will play a role in some of the proposed methods to

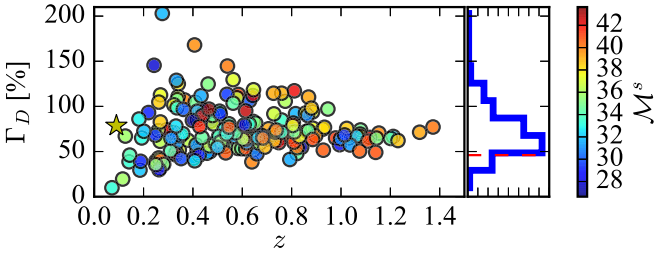

FIG. 18. The distribution of the 90% CI relative uncertainty (in percent over the true value) in the estimation of the luminosity distance (y axis) against the true redshift (x axis). The color bar is the source-frame chirp mass of the simulated signals, in solar masses. A star reports the coordinates of GW150914. The dashed line on the histogram marks the abscissa of the 10th percentile.

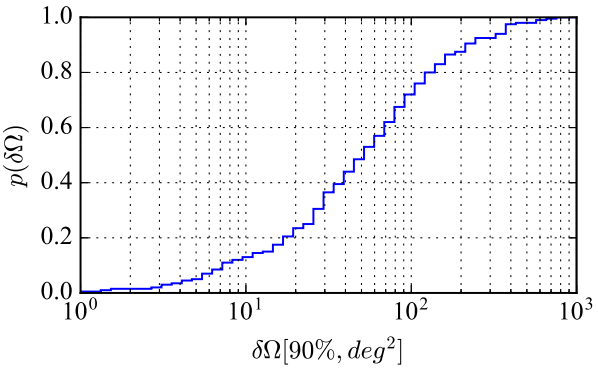

FIG. 19. Cumulative distribution for the 90% CI sky localization area for BBH detected by the HLV network.

calculate cosmological parameters with gravitational waves and to pinpoint the host a galaxy of CBC sources [65–67].

In Fig. 18 we show the relative 90% CI uncertainty against the true redshift; the color reports the true source-frame chirp mass. We see that uncertainties have scatter for low distances and then converge toward values of around 50%. A rough Fisher-matrix-based approach would suggest that the relative errors should only depend on the SNR [49,68]. Since for large redshifts most events will have similar SNR (corresponding to the threshold value we used to consider an event "detected"), that explains why the points converge to a similar value.

We find that the uncertainties peak at ∼50%, slightly below what was found for GW150914.

We should stress that we are only reporting statistical uncertainties in the luminosity distance. As LIGO and Virgo start to detect sources at non-negligible redshifts, weak lensing could affect distance measurement. This potential systematic effect has already been investigated in the context of third-generation gravitational wave detectors, such as the Einstein Telescope [69] or the Cosmic Explorer [70,71]. Following [66], we can assume that weak lensing could introduce a systematic of ∼5% on the luminosity distance measurement for sources at $z = 1$, and smaller for sources at smaller redshifts. For all the sources in our study, this potential systematic effect would thus be much smaller than the statistical uncertainty.

While unlikely, it is not impossible that BBH will in fact emit energy in the electromagnetic band, or neutrinos, as some mechanisms have been proposed [72,73] after the discovery of GW150914 and the potential electromagnetic subthreshold trigger found by the Fermi mission [74]. Furthermore, it could be possible to use the position of detected events to study the large-scale structure of the Universe [75,76] and to look for the host galaxy and calculate the cosmological parameters [65].

In Fig. 19 we show cumulative distributions for the 90% credible interval for the sky position, in square degrees. In our runs we have not included marginalization over instrumental calibration uncertainties, which have the potential to increase the sky uncertainties [4,6] or to bias it, if not accounted for [77]. We have implicitly assumed that by the time the advanced detectors reach design sensitivity, calibration uncertainties, which are now at a ∼5% level [4,78], will be better understood.

Our results are comparable with [79], which focused on binary neutron stars. The main difference is that the uncertainties we obtain for BBH are larger than what they obtained for binary neutron stars, in spite of the fact that we quote 90% CI, while they used 95% CI.

For example, for the HLV network (Notice that Ref. [79] considered an advanced network with Virgo, LIGO Livingston, and two LIGO Hanford interferometers. That network will not be realized since one of the two LIGO Hanford detector is being relocated to India) we obtain a median uncertainty of 50 deg^2, while [79] obtains ∼30 deg^2.

This is, of course, due to the fact that BBH signals have a smaller effective bandwidth [80] and are hence harder to localize than longer binary neutron star sources [81].

Finally, it is worth mentioning that the sky maps shared with partner astronomers for prompt follow-up are currently produced by a low-latency algorithm (BAYESTAR [82]), while `lalinference` sky maps, which include a more detailed model of the source and instrument calibration, follow with a higher latency. It has been shown that the low and medium latency maps are in very good agreement for a network of two instruments, while the agreement is lower for a three-instrument network because `lalinference` is able to use data from all three detectors regardless of the presence of a trigger [83]. This discrepancy is currently being addressed in preparation for Advanced Virgo's first observing run [84] (see Sec. X of [82]). Reference [83] deals with binary neutron stars, but the situation should be similar for BBH, unless significant spin precession is present. In that case `lalinference` should provide a more accurate sky map since the low-latency algorithm is based on the output of search pipelines which currently neglect precession.

IV. TRENDS

In the previous section we have focused on an astrophysical population of events and obtained distributions for the expected uncertainties of the sources' parameters. We now want to show how the estimation of the spin parameters depends on the intrinsic parameters of the source (i.e., mass and spin) as well as on its orientation.

A. Dependence on orientation

It is commonly assumed that in the limit of spins aligned with the orbital angular momentum, the spin parameters are strongly degenerate with the mass ratio for small masses [85] and are hence hard to measure. Mathematically, this happens because the leading order spin term in the waveform inspiral phase depends on a combination of mass ratio and (aligned) spins. At the same time, when misaligned spins are present, spin-spin and spin-orbit interactions will make the orbital plane precess, which gives the signal amplitude and phase modulation [86]. One would thus think that precessing spins are easier to measure. Since the amount of precession visible at Earth is also a function of the inclination angle [6,22,86], the best-case scenario should be when precession is present and the system is observed from "edge-on" (orbital angular momentum forming an angle of $\pi/2$ with the line of sight). In [22] it was shown, for one particular low-mass BBH system, how uncertainties in the measurement of spin do indeed reach a minimum for inclination angles close to $\pi/2$.

However, as underlined by Ref. [85], there is no reason the known degeneracies of the inspiral phase should hold true when the merger and ringdown parts of the waveform are measurable.

In this section we investigate how the characterization of heavy BBH sources depends on the orientation of the systems and their spins.

We consider several systems with different values of masses, spin orientation and SNR, and analyze them for different values of inclination angle (to be exact, what we have varied is the angle between the total angular momentum and the line of sight, θ_{JN} [5,87]). The parameters of the sources we used are reported in Table I. We consider mass ratios from 1 to 1:2.5, and mostly focus on large spins. Tilt angles are typically chosen to be large so that precessional effects are seen in the first place.

TABLE I. Intrinsic parameters and network SNRs for the systems of Fig. 20. Masses are in $M_\odot$.

	a_1,a_2	m_1,m_2	SNR	$\cos\tau_1$, $\cos\tau_2$	Marker
q1a	0.9, 0.9	35, 35	17	0.5, 0.5	♦
q1b	0.9, 0.2	35, 35	25	0.8, 0.5	♦
q1d5	0.9, 0.9	45, 30	17	0.5, 0.5	×
q1d5ss	0.4, 0	45, 30	17	0.5, 0.5	×
q2a	0.9, 0.9	70, 35	17	0.5, 0.5	■
q2d5	0.9, 0.9	75, 30	17	0.5, 0.5	▼
q1ali	0.9, 0.9	35, 35	17	1,1	♣
q2ali	0.9, 0.9	70, 35	17	1, 1	♠

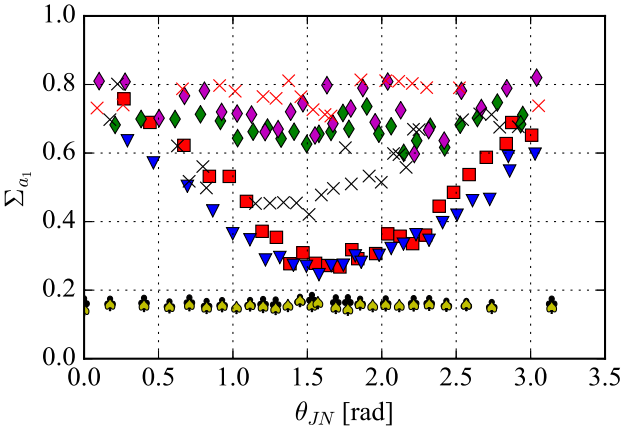

FIG. 20. The 90% CI uncertainty in the primary spin magnitude against θ_{JN} (rads) for various BBH sources. See Table I for the parameters of the sources.

We stress that every time a system is rotated, its distance is varied to keep the same SNR. The variations we see are thus not due to variations in the loudness of the source, but only on the extra complexity of the signal when not face-on. In Fig. 20 we report the 90% CI uncertainty for the primary spin against θ_{JN}.

We see that the effect strongly depends on the mass ratio of the systems. For equal-mass sources (diamonds) we do not see any strong variation on the ability to measure the spin magnitude. This is compatible with the fact that spin-induced modulation effects are minimal for equal-mass systems [35]. As the mass ratio increases, so does the effect of the inclination angle. For the source with mass ratio 1:1.5 (crosses), we start to observe a reduction of the uncertainties for large inclination angles, unless the spins are small.

The improvement is even more pronounced for the sources with mass ratios of 2 (squares) and 2.5 (triangles). For these sources, as expected, uncertainties reach their minimum for angles close to $\pi/2$. Furthermore, we see that the ratio between uncertainties in the best- and worst-case scenarios can be over a factor of 2. Although in this paper we do not deal with neutron star–black hole binaries, the ratio would be even larger for those sources given their larger mass ratio. We stress that by using IMRPhenomPv2 for large inclination angles, we are in fact working on a corner of the parameter space where that approximant might not be highly reliable [36]. The fact that the curves we obtain look similar to those reported in [22] using a different approximant (SpinTaylorT4 [88,89]) and lower masses reassures us that the results we find in this section are at least a good indication of the trends one can expect. Of course, a similar study should be repeated as soon as fast double-spinning IMR waveforms become available.

Potential systematics against numerical relativity waveforms should also be quantified.

We now want to verify if aligned spins are harder to measure even for heavy BBH, for which merger and ringdown are in band. In Fig. 20 we show results for two spin-aligned BBH, with mass ratios of 1 (black club suits) and 2 (yellow spade suits). In both cases, the spins are 0.9 (see Table I). We stress that while the simulated BBH had aligned spins, the parameter estimation algorithm did *not* make this assumption; i.e., we explored the full precessing parameter space. We see that the uncertainties in this case are considerably smaller than all other precessing systems we considered, at around 0.2.

As mentioned above, it has been stressed elsewhere [85] that one should not *a priori* expect the same correlations found in inspiral-dominated (i.e., low-mass) systems to hold true for heavy BBH. This is also consistent with the fact that for large and aligned spins, the length of a waveform is increased [90]. While this effect would be degenerate with the total mass if only the inspiral phase were in band, the presence of a measurable merger and ringdown breaks that degeneracy, improving the measurability of spin parameters.

We have verified that these results hold true if (a) the template used for parameter estimation only considers aligned spin and (b) the simulated signals are not exactly aligned but have tilt angles of ∼3–5 degrees.

We thus find that uncertainties for spin-aligned heavy BBH can be much smaller than for precessing systems of similar masses if significant spin is present. Our finding that spins nearly aligned with the orbital angular momentum can be estimated very well when the merger and ringdown are in band is compatible with what was found in [54], which used a different waveform family.

B. Dependence on mass

The results of the previous section have shown how characterization of heavy BBH might have properties that were not previously thoroughly discussed or investigated. In this section we want to investigate another common assumption, that heavier CBCs are harder to characterize, being shorter in both the time and the frequency domain.

We consider two precessing systems with fixed mass ratios of 1 (red squares) and 2 (green diamonds) and a spin-aligned system with a mass ratio of 1 (black club suits). Their parameters are given in Table II.

TABLE II. Intrinsic parameters and network SNRs for the systems of Fig. 21. Masses are in $M_\odot$, and θ_{JN} is 45 deg for all systems.

	a_1,a_2	q	SNR	$\cos\tau_1$, $\cos\tau_2$	Marker
q1	0.9, 0.9	1	17	0.5, 0.5	■
q2	0.9, 0.9	2	17	0.5, 0.5	♦
q1ali	0.9, 0.9	1	17	1,1	♣

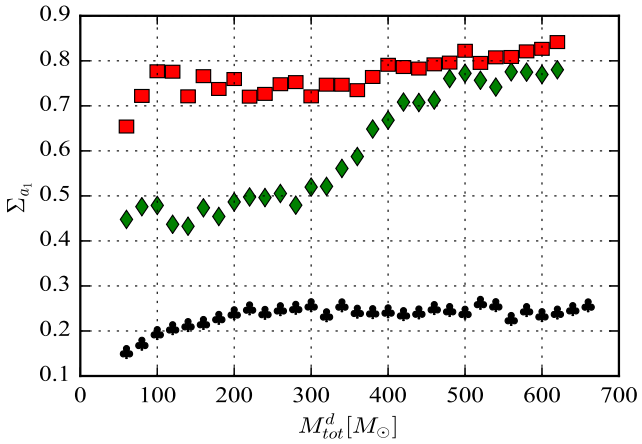

FIG. 21. The 90% CI uncertainty in the primary spin magnitude against the detector frame total mass. See Table II for the parameters.

These systems were simulated with increasingly large detector frame total mass. Every time the total mass if varied, the distance to the source is also changed to yield the same network SNR for all masses. Recall that when spin-induced orbital precession is present, some spin parameters become time, and hence frequency, dependent. Throughout this work we have defined spin parameters, such as the tilt angles, at 20 Hz. However, in this section we make a different choice. To ensure that spins are defined at fixed numbers of cycles before merger, we define spins at a different reference frequency for each value of mass. To be precise, for each $M_{\rm tot}$ the spins are defined at a reference frequency, such that $M_{\rm tot} f_{\rm ref} = \text{const}$.

We first look at the estimation of the magnitude of the primary spin. In Fig. 21 we show the 90% CI for the primary spin magnitude versus the redshifted total mass. We see how, while the overall trend is an increase of the uncertainties with the total mass, the amount of variation depends on the mass ratio. The precessing equal-mass system (red squares) shows the smallest variation, with uncertainties which are significantly large already at small masses. On the other hand, the system with a mass ratio of 2 has mild uncertainties at $M = 60\ \mathrm{M}_\odot$ which increase by a factor of 2 as the total mass increases to $M = 600\ \mathrm{M}_\odot$. Remarkably, the uncertainties for the spin-aligned system (club suits) stay much smaller than the precessing spin systems in the whole mass range.

Next, we report the uncertainties on the measurement on the effective spin along the orbital angular momentum. As we have seen above, the effective spin parameter can generally be estimated more precisely than either component spin. We find this is the case for all values of masses we consider, at least for the precessing systems (Fig. 22). For the spin-aligned system we see that the uncertainty in $\chi_{\rm eff}$ is similar to the uncertainty in a_1, which is not

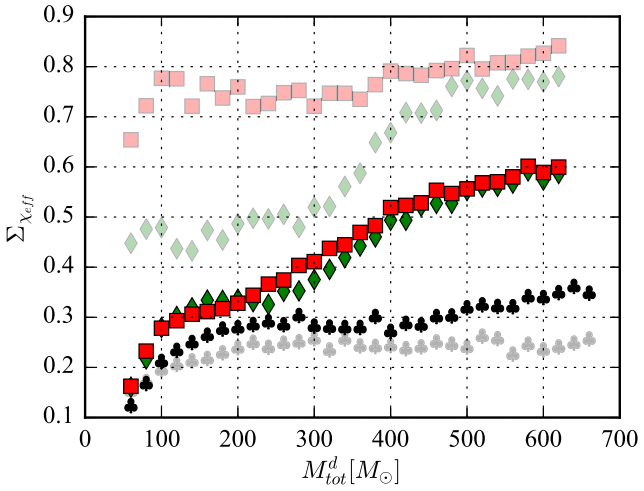

FIG. 22. The 90% CI uncertainty in the effective spin along the orbital angular momentum against the detector frame total mass. The uncertainties in primary spin magnitude are also shown (semitransparent symbols) for reference. See Table II for the parameters.

surprising since the whole spin is along the orbital angular momentum and hence contributes to the effective spin.

We notice that the uncertainty in the estimation of $\chi_{\rm eff}$ is similar among the two precessing systems, while we observe large differences in the measurement of the primary spin magnitude (Fig. 21). This is due to the fact that the measurements of the component spin magnitude are also affected by the correlation of spin magnitude with spin orientation, which depends on how much precession is "visible." We thus look at the estimation of the effective precessing spin, χ_p, i.e., a mass-weighted combination of

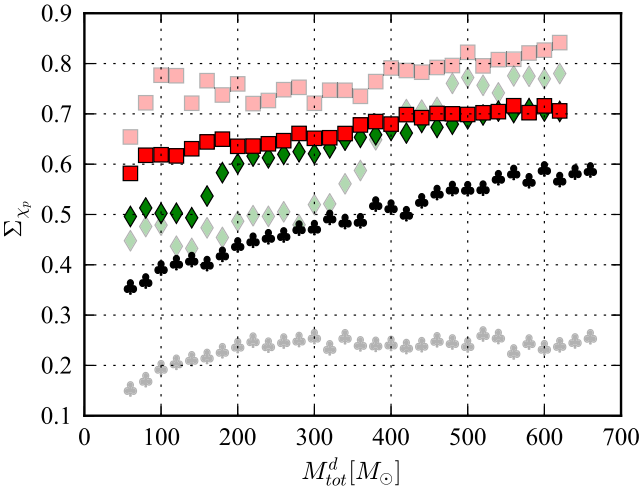

FIG. 23. The 90% CI uncertainty in the effective spin along the plane of the orbit against the detector frame total mass. The uncertainties in primary spin magnitude are also shown (semitransparent symbols) for reference. See Table II for the parameters.

the total spin component in the plane of the orbit. As for $\chi_{\rm eff}$, motivation for the use of this parametrization has been discussed elsewhere [55–60]. This is shown in Fig. 23.

We see that, especially for low masses, the $q = 2$ system has smaller uncertainties for χ_p than the precessing equal-mass source. This is due to the fact that, as mentioned above, precession effects are more visible when a mass asymmetry exists. We have verified that the small jump in uncertainty for $M \sim 150$ $\mathrm{M}_\odot$ for the $q = 2$ system happens as the peak of the first precession cycle (i.e., the one at lower frequency) starts going out of band, due to the increasing total mass. We notice that for χ_p too, the spin-aligned systems have smaller uncertainties. However, the uncertainties for spin-aligned systems are not smaller because their spins are measured better than for the precessing systems. Quite the contrary, we find that the posterior for χ_p is centered at ~0.4 for most spin-aligned runs (the injected value is 0.0), not far from where the prior is centered. We notice, however, that the posterior for the spin-aligned runs is slightly narrower than the prior.

V. CHARACTERIZATION OF MASS AND SPIN DISTRIBUTION

Although measuring the spins of *single* objects will be hard, we stress that it will be possible to learn something about the underlying population by combining information from several sources. For example, in Fig. 11 we have seen how one can very often discard large values of spins if the true distribution has smaller spin values. In that case, one can imagine how, as more detections are made, large spins become less and less supported by the data.

In this section we use a very simple toy model to show how inference about the mass and spin distributions can be done. Let us consider a set of 105 BBH with masses uniformly distributed in the range $[30, 50]$ $\mathrm{M}_\odot$ and spins uniformly distributed in $a \in [0.7, 0.98]$. Under the hypothesis that mass and spin distributions are flat, with unknown boundaries, can the extrema be estimated? If yes, how many detections are needed?

Let us start by estimating the boundaries of the component mass distribution. Here, $m_{\rm min}$ and $m_{\rm max}$ are the minimum and maximum of the astrophysical distribution, and $\mathcal{H}$ is the model in which the distribution is flat. If N detections are made, symbolized by their data streams $\vec{d}$, then using Bayes' theorem one can write

$$\begin{aligned} p(m_{\rm min}, m_{\rm max}|\vec{d},\mathcal{H}) &\propto p(m_{\rm min}, m_{\rm max}|\mathcal{H})\, p(\vec{d}|m_{\rm min}, m_{\rm max},\mathcal{H}) \\ &= p(m_{\rm min}, m_{\rm max}|\mathcal{H}) \prod_{i=1..N} p(d^i|m_{\rm min}, m_{\rm max},\mathcal{H}), \end{aligned} \tag{2}$$

where d^i is the data stream of the ith signal.

Each term in the product is just the usual evidence of the data, but restricted to mass values between the min and max being considered. This can be implemented trivially in the parameter estimation algorithm we used by restricting the

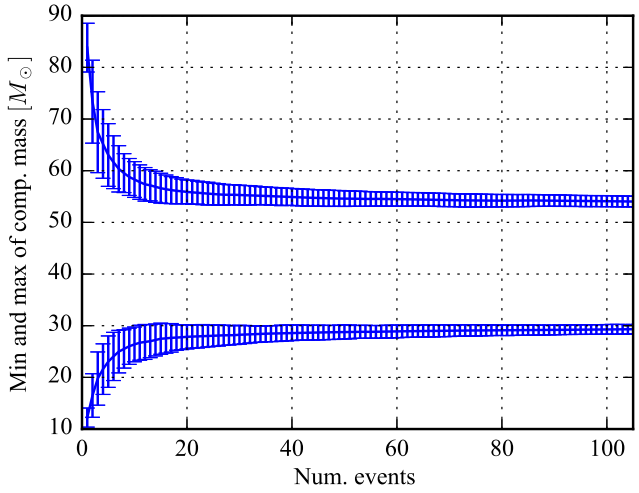

FIG. 24. The estimation of the minimum and maximum values of the component mass for a population of BBH as more events are detected. The error bars are obtained by bootstrapping 100 sets of N events for each value of N, in the x axis. The true distribution is flat between 30 $M_\odot$ and 50 $M_\odot$ for both masses. After 20 events, we can confidently measure the edges of the underlying mass distribution.

prior range of the component masses [5]. In practice, to avoid wasting computational resources and since the original priors are flat, we just use importance sampling [91]. The other term in the rhs is the prior distribution for the minimum and maximum, which we can take as flat.

In Fig. 24 we show how the estimation of the minimum and maximum range for the source-frame component masses evolves as more events are detected. The x axis reports the number of events used, and the y axis shows the estimated values of the maximum (upper curve) and minimum (bottom curve). To calculate error bars, for each choice of the number of events, N, we generated 100 random sets of N events with bootstrapping and calculated mean and standard deviation of the edges of the 90% credible interval.

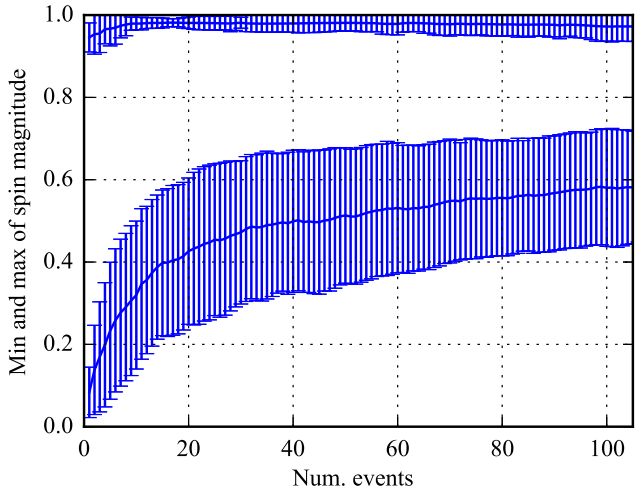

FIG. 25. The estimation of the minimum and maximum values of the spin magnitude for a population of BBH as more events are detected. The error bars are obtained by bootstrapping 100 sets of N events for each value of N, in the x axis. The true distribution is flat between 0.7 and 0.98. After 20 events, we can exclude nonspinning BBH in the underlying astrophysical population.

The same exercise can be done for the spin magnitude. Using the same expression we derived for the masses, one obtains the joint distribution for $a_{\rm min}$ and $a_{\rm max}$. In Fig. 25 we show the evolution of the estimation for $a_{\rm min}$ and $a_{\rm max}$ as a function of detected events.

We see that the error bars are much larger than for the masses, which is simply a consequence of the fact that spins are harder to measure than masses. After 10–20 events, nonspinning BBH are excluded, and after a few tens of events, the data points to a minimum spin at around 0.6, with standard deviations of ∼0.1.

The results of this section should be seen as the simple application of a toy model and are only meant to give the reader an idea of what can be done when several sources are available. Here, we list three main caveats. The number of sources that are needed to, e.g., exclude negligible spins are of course dependent on our choice of population, of which we consider one possibility. For example, if the true population had spins down to, e.g., 0.4 rather than 0.7, then more sources would be needed. Furthermore, the true astrophysical distribution of spins and masses would not have sharp boundaries, and its shape would not be known. Measuring the edges of a flat (top-hat) distribution leads to better results than estimating the parameters of more realistic distributions (e.g., Gaussian, power law).[2] An example of a more elaborate treatment in the context of population modeling can be found in [92], which appeared after we started this work. Finally, as mentioned in Sec. II B, the IMRPhenomPv2 approximant may not be able to accurately compute the gravitational waveform for the few edge-on [29,43], low SNR, signals in the population.

VI. CONCLUSIONS

In this paper we have considered an astrophysical distribution of heavy ($m_{1,2} \in [30, 50]$ $M_\odot$) spinning BBH detected by a network of advanced LIGO and Virgo detectors. Sources like these will be detected in high numbers in the next few years, and it is interesting to verify what kind of measurement one can expect for the masses and spins of black holes in these systems.

We find that source-frame component masses will be estimated with typical relative uncertainties of the order of ∼40%. The exact size of the errors will depend on, besides the signal-to-noise ratio, the detector-frame masses since

[2]We thank Will Farr for clarifying this point.

those control the duration and amplitude of the signal. There will thus be a coupling between source-frame mass estimation and source redshift. This correlation will be exacerbated in the next generation of gravitational wave detectors [28]. The source-frame chirp mass is estimated with similar precision.

The spin magnitude of either object in the binary will typically be estimated with large uncertainties. We found that for the primary (i.e., most massive) object in the system, only 10% of sources will yield a measurement with uncertainty below 0.7. For the secondary, that number is 0.85. We found that large spins can typically be estimated with smaller uncertainties, similarly to what happens for BH in x-ray binaries. The effective spin along the orbital angular momentum, $\chi_{\rm eff}$, can be measured better than either spins, with uncertainties for 10% of sources below 0.17.

Considering only the BBH in our population with primary spin below 0.2, we saw that ∼90% of the time, one can exclude that the BH was fast spinning (i.e., with spin above 0.95). This number goes down to roughly 80% if a flat distribution of spin is used. Conversely, if only BBH with primary spin above 0.8 are used, 75% of them will not support negligible spins (i.e., spin below 0.05). If the whole flat spin distribution is used, 55% of the systems will exclude negligible spins. We have checked how well the sign of the effective spin can be measured, which could be used to prefer some formation models for CBCs. We have found that if one only considers BBH with $\chi_{\rm eff} < -0.3$ ($\chi_{\rm eff} > +0.3$) 70% (80%) of the time, one can exclude positive (negative) $\chi_{\rm eff}$.

The angle between spin and orbital angular momentum, which could also be used to probe the formation channels of CBC, will be estimated quite poorly as well. For only 6% of our BBH, the 90% CI for this angle is below 60°.

We have verified that the uncertainties of GW150914 for both masses and spins are typical of events in the same mass range. We have shown how correlations can exist between the ability of measuring the spin parameters, for precessing systems, and the inclination of the orbit. However, these correlations are only clear if the mass ratio is not close to unity. For equal mass systems, precessing spins are hard to measure no matter what the orientation of the orbit is. We considered spin-aligned systems with mass ratios of 1 and 2 and spin magnitude of 0.9, and we found that the spin magnitude can be measured extremely well, with 90% CI of ∼0.2. This is contrary to what is traditionally expected for low-mass CBCs, which are dominated by the inspiral phase and show a strong degeneracy between spin and mass ratio.

We then investigated how the uncertainties on the spin magnitude depend on the detector-frame total mass. We found that while uncertainties become larger overall for larger masses, the increase is much more significant when the mass ratio is not close to unity. For the system with mass ratio of 2 that we considered, the uncertainty in the primary spin magnitude at $M_{\rm tot} = 60\ {\rm M}_\odot$ is a factor of 2 smaller than at $M_{\rm tot} = 600\ {\rm M}_\odot$.

Finally, we have verified what can be said about the mass and spins of the underlying distribution of BBH events. Considering a toy model where masses are uniform in the range $[30\text{–}50]\,{\rm M}_\odot$ and spins are uniform in the range [0.7–0.98], we have shown how the boundaries can be measured assuming a top-hat distribution, with less than 100 detections. A top-hat distribution is of course only a crude approximation, and more work will be needed to assess the characterization of more realistic distributions.

ACKNOWLEDGMENTS

The authors would like to thank T. Dent, D. Gerosa, V. Kalogera, M. Pürrer, C. Rodriguez, R. O'Shaughnessy, and the LSC-Virgo parameter estimation subgroup for useful discussion and comments. We also thank the referee for many useful comments. S. V. and R. L. acknowledge the support of the National Science Foundation and the LIGO Laboratory. LIGO was constructed by the California Institute of Technology and Massachusetts Institute of Technology with funding from the National Science Foundation, and it operates under Cooperative Agreement No. PHY-0757058. J. V. was supported by STFC Grant No. ST/K005014/1. During this work, R. S. was supported by FAPESP Grants No. 2012/14132-3, No. 2013/04538-5, and No. 2014/50727-7. The authors would like to acknowledge the LIGO Data Grid clusters, without which the simulations could not have been performed. Specifically, we thank the Albert Einstein Institute in Hannover, supported by the Max-Planck-Gesellschaft, for use of the Atlas High-Performance Computing Cluster. We are also grateful for computational resources provided by the Leonard E. Parker Center for Gravitation, Cosmology and Astrophysics at University of Wisconsin-Milwaukee. This is LIGO Document P1600292.

APPENDIX: FIVE-DETECTOR NETWORK

In this appendix we report results on a different BBH population, with intrinsic component masses flat in the range $[25\text{–}100]\ {\rm M}_\odot$ (and $M_{\rm tot} \leq 100\ {\rm M}_\odot$) as detected by a five-detector network which includes the two LIGO, Virgo, KAGRA and LIGO India (henceforth HVLIJ). The main goal of this section is to show that, if an astrophysical distribution of BBH of roughly similar masses is considered, the actual configuration of the network does not matter, in the first approximation, for the measurement of the intrinsic parameters. We will in fact see that the uncertainties we obtain with the HLVIJ network are similar, for masses and spins, to what we reported in the main body of the paper for the smaller HLV network.

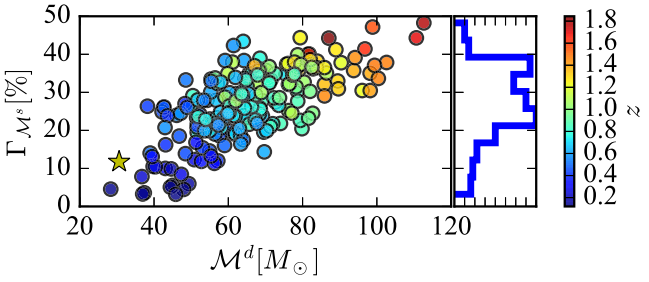

FIG. 26. For an HLVIJ network, the distribution of the 90% CI relative uncertainty (in percent over the true value) in the estimation of the source-frame chirp mass (y axis) against the true source-frame chirp mass (x axis). The color bar is the redshift of the sources. A star reports the coordinates of GW150914.

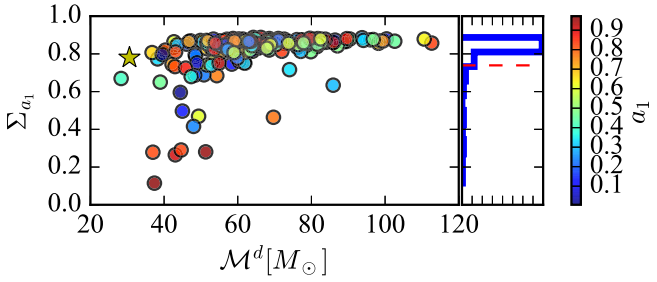

FIG. 27. For an HLVIJ network, the distribution of the 90% CI uncertainty in the estimation of the primary spin magnitude (y axis) against the true detector-frame chirp mass (x axis). The color bar shows the magnitude of the primary spin. A star reports the coordinates of GW150914.

Let us start with the relative uncertainties in the source-frame chirp mass (Fig. 26). Comparing with the corresponding plot for the HLV network, Fig. 5, we see that uncertainties are similar, and mostly around ∼30%. The bulk of the distribution is slightly larger for HLVIJ because more events with high redshifted mass are detected by this network, owing to its larger range.

We will not plot the distribution of uncertainties for m_1 and m_2; we just mention that they too look very similar to the corresponding HLV curves. In particular, the relative source-frame m_1 (m_2) uncertainty peaks at ∼45% (∼50%), which is slightly more than for HLV, for the reasons just mentioned above. In Fig. 27 we show instead the uncertainties for the spin magnitude of the primary. We still find that large errors will be common, with only 10% of the systems having 90% CI below 0.73 (basically the same as HLV, for which we obtained 0.70). Once again, measurement is harder for the spin of the secondary object; 90% of the sources will have uncertainties above 0.86—i.e., they will be unmeasurable.

Figure 27 also shows that the measurement of spins gets worse for systems with large (redshifted) mass. We have seen in Sec. IV B how this is indeed the case.

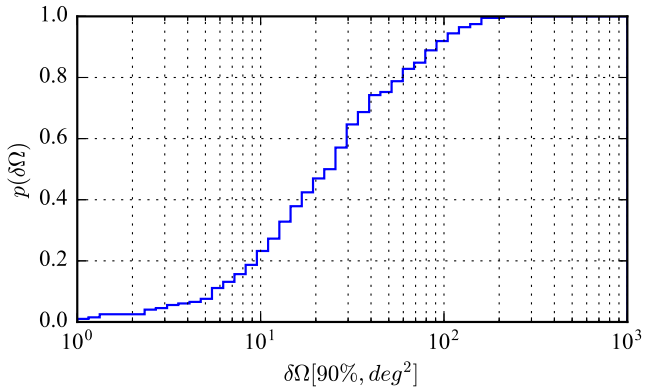

FIG. 28. Cumulative distribution for the 90% CI sky localization area for BBH detected by the HLVIJ network.

We end this appendix by mentioning that, as one would expect, sky localization gets better with the five-detector network. Using the same figure of merit of Sec. III C, we find that the median sky localization uncertainty is ∼25 deg^2, i.e., a factor of ∼2 smaller than what was obtained with the HLV network (Fig. 28).

[1] G. M. Harry (LIGO Scientific Collaboration), Classical Quantum Gravity **27**, 084006 (2010).
[2] B. P. Abbott, R. Abbott, T. D. Abbott *et al.* (LIGO Scientific Collaboration and Virgo Collaboration), Phys. Rev. Lett. **116**, 061102 (2016).
[3] B. P. Abbott, R. Abbott, T. D. Abbott, M. R. Abernathy, F. Acernese, K. Ackley, C. Adams, T. Adams, P. Addesso, R. X. Adhikari *et al.*, Phys. Rev. Lett. **116**, 241103 (2016).
[4] B. P. Abbott *et al.* (LIGO Scientific Collaboration and Virgo Collaboration), Phys. Rev. X **6**, 041015 (2016).
[5] J. Veitch, V. Raymond, B. Farr, W. Farr, P. Graff, S. Vitale, B. Aylott, K. Blackburn, N. Christensen, M. Coughlin *et al.*, Phys. Rev. D **91**, 042003 (2015).
[6] B. P. Abbott, R. Abbott, T. D. Abbott, M. R. Abernathy, F. Acernese, K. Ackley, C. Adams, T. Adams, P. Addesso, R. X. Adhikari *et al.*, Phys. Rev. Lett. **116**, 241102 (2016).
[7] B. P. Abbott, R. Abbott, T. D. Abbott, M. R. Abernathy, F. Acernese, K. Ackley, C. Adams, T. Adams *et al.* (LIGO Scientific Collaboration and Virgo Collaboration), Phys. Rev. X **6**, 041014 (2016).

[8] B. P. Abbott, R. Abbott, T. D. Abbott, M. R. Abernathy, F. Acernese, K. Ackley, C. Adams, T. Adams, P. Addesso, R. X. Adhikari *et al.*, Phys. Rev. Lett. **116**, 221101 (2016).

[9] N. Yunes, K. Yagi, and F. Pretorius, Phys. Rev. D **94**, 084002 (2016).

[10] A. Vikhlinin, Astrophys. J. Lett. **521**, L45 (1999).

[11] F. Özel, D. Psaltis, R. Narayan, and J. E. McClintock, Astrophys. J. **725**, 1918 (2010).

[12] S. N. Zhang, W. Cui, and W. Chen, Astrophys. J. Lett. **482**, L155 (1997).

[13] A. C. Fabian, M. J. Rees, L. Stella, and N. E. White, Mon. Not. R. Astron. Soc. **238**, 729 (1989).

[14] C. S. Reynolds and M. A. Nowak, Phys. Rep. **377**, 389 (2003).

[15] J. E. McClintock, R. Narayan, S. W. Davis, L. Gou, A. Kulkarni, J. A. Orosz, R. F. Penna, R. A. Remillard, and J. F. Steiner, Classical Quantum Gravity **28**, 114009 (2011).

[16] B. P. Abbott, R. Abbott, T. D. Abbott *et al.* (LIGO Scientific Collaboration and Virgo Collaboration), Astrophys. J. Lett. **818**, L22 (2016).

[17] B. P. Abbott, R. Abbott, T. D. Abbott *et al.* (LIGO Scientific Collaboration and Virgo Collaboration), Astrophys. J. Lett. **833**, L1 (2016).

[18] B. P. Abbott, R. Abbott, T. D. Abbott, M. R. Abernathy, F. Acernese, K. Ackley, C. Adams, T. Adams, P. Addesso, R. X. Adhikari *et al.*, Living Rev. Relativ. **19** (2016).

[19] S. Vitale, Phys. Rev. D **94**, 121501 (2016).

[20] A. Ghosh, W. Del Pozzo, and P. Ajith, Phys. Rev. D **94**, 104070 (2016).

[21] C. Pankow, L. Sampson, L. Perri, E. Chase, S. Coughlin, M. Zevin, and V. Kalogera, Astrophys. J. **834**, 154 (2017).

[22] S. Vitale, R. Lynch, J. Veitch, V. Raymond, and R. Sturani, Phys. Rev. Lett. **112**, 251101 (2014).

[23] V. Raymond, M. V. van der Sluys, I. Mandel, V. Kalogera, C. Röver, and N. Christensen, Classical Quantum Gravity **26**, 114007 (2009).

[24] M. V. van der Sluys, C. Röver, A. Stroeer, V. Raymond, I. Mandel, N. Christensen, V. Kalogera, R. Meyer, and A. Vecchio, Astrophys. J. **688**, L61 (2008).

[25] K. Somiya, Classical Quantum Gravity **29**, 124007 (2012).

[26] B. Iyer *et al.* https://dcc.ligo.org/cgi-bin/DocDB/ShowDocument?docid=75988.

[27] F. Acernese *et al.* (Virgo Collaboration), Classical Quantum Gravity **32**, 024001 (2015).

[28] S. Vitale and M. Evans, preceding paper, Phys. Rev. D **95**, 064052 (2017).

[29] S. Vitale, Phys. Rev. D **94**, 121501 (2016).

[30] P. A. R. Ade, N. Aghanim, M. Arnaud, M. Ashdown, J. Aumont, C. Baccigalupi, A. J. Banday, R. B. Barreiro, J. G. Bartlett *et al.* (Planck Collaboration), Astron. Astrophys. **594**, A13 (2016).

[31] B. P. Abbott, R. Abbott, T. D. Abbott *et al.* (LIGO Scientific Collaboration and Virgo Collaboration), Phys. Rev. Lett. **116**, 131103 (2016).

[32] M. Hannam, P. Schmidt, A. Bohé, L. Haegel, S. Husa, F. Ohme, G. Pratten, and M. Pürrer, Phys. Rev. Lett. **113**, 151101 (2014).

[33] S. Khan, S. Husa, M. Hannam, F. Ohme, M. Pürrer, X. J. Forteza, and A. Bohé, Phys. Rev. D **93**, 044007 (2016).

[34] S. Husa, S. Khan, M. Hannam, M. Pürrer, F. Ohme, X. J. Forteza, and A. Bohé, Phys. Rev. D **93**, 044006 (2016).

[35] P. Schmidt, F. Ohme, and M. Hannam, Phys. Rev. D **91**, 024043 (2015).

[36] LIGO Collaboration and Virgo Collaboration (unpublished).

[37] M. Pürrer, Phys. Rev. D **93**, 064041 (2016).

[38] M. Pürrer, Classical Quantum Gravity **31**, 195010 (2014).

[39] J. Blackman, B. Szilagyi, C. R. Galley, and M. Tiglio, Phys. Rev. Lett. **113**, 021101 (2014).

[40] S. E. Field, C. R. Galley, J. S. Hesthaven, J. Kaye, and M. Tiglio, Phys. Rev. X **4**, 031006 (2014).

[41] P. Canizares, S. E. Field, J. Gair, V. Raymond, R. Smith, and M. Tiglio, Phys. Rev. Lett. **114**, 071104 (2015).

[42] R. Smith, S. E. Field, K. Blackburn, C.-J. Haster, M. Pürrer, V. Raymond, and P. Schmidt, Phys. Rev. D **94**, 044031 (2016).

[43] B. F. Schutz, Classical Quantum Gravity **28**, 125023 (2011).

[44] M. van der Sluys, I. Mandel, V. Raymond, V. Kalogera, C. Röver, and N. Christensen, Classical Quantum Gravity **26**, 204010 (2009).

[45] J. Veitch and A. Vecchio, Phys. Rev. D **81**, 062003 (2010).

[46] C. L. Rodriguez, B. Farr, V. Raymond, W. M. Farr, T. B. Littenberg, D. Fazi, and V. Kalogera, Astrophys. J. **784**, 119 (2014).

[47] S. Vitale and W. Del Pozzo, Phys. Rev. D **89**, 022002 (2014).

[48] B. Farr, C. P. L. Berry, W. M. Farr, C.-J. Haster, H. Middleton, K. Cannon, P. B. Graff, C. Hanna, I. Mandel, C. Pankow *et al.*, Astrophys. J. **825**, 116 (2016).

[49] K. G. Arun, B. R. Iyer, B. S. Sathyaprakash, and P. A. Sundararajan, Phys. Rev. D **71**, 084008 (2005).

[50] J. Veitch, M. Pürrer, and I. Mandel, Phys. Rev. Lett. **115**, 141101 (2015).

[51] P. B. Graff, A. Buonanno, and B. S. Sathyaprakash, Phys. Rev. D **92**, 022002 (2015).

[52] C.-J. Haster, Z. Wang, C. P. L. Berry, S. Stevenson, J. Veitch, and I. Mandel, Mon. Not. R. Astron. Soc. **457**, 4499 (2016).

[53] C. L. Rodriguez, S. Chatterjee, and F. A. Rasio, Phys. Rev. D **93**, 084029 (2016).

[54] M. Pürrer, M. Hannam, and F. Ohme, Phys. Rev. D **93**, 084042 (2016).

[55] M. Pürrer, M. Hannam, P. Ajith, and S. Husa, Phys. Rev. D **88**, 064007 (2013).

[56] T. Damour, Phys. Rev. D **64**, 124013 (2001).

[57] P. Ajith, Phys. Rev. D **84**, 084037 (2011).

[58] E. Racine, Phys. Rev. D **78**, 044021 (2008).

[59] P. Ajith, M. Hannam, S. Husa, Y. Chen, B. Brügmann, N. Dorband, D. Müller, F. Ohme, D. Pollney, C. Reisswig, L. Santamaría, and J. Seiler, Phys. Rev. Lett. **106**, 241101 (2011).

[60] L. Santamaría, F. Ohme, P. Ajith, B. Brügmann, N. Dorband, M. Hannam, S. Husa, P. Mösta, D. Pollney, C. Reisswig, E. L. Robinson, J. Seiler, and B. Krishnan, Phys. Rev. D **82**, 064016 (2010).

[61] C. L. Rodriguez, M. Zevin, C. Pankow, V. Kalogera, and F. A. Rasio, Astrophys. J. Lett. **832**, L2 (2016).

[62] S. Vitale, R. Lynch, R. Sturani, and P. Graff, Classic Quantum Gravity **34**, 03LT01 (2017).

[63] V. Kalogera, Astrophys. J. **541**, 319 (2000).

[64] C. L. Rodriguez, M. Zevin, C. Pankow, V. Kalogera, and F. Rasio (unpublished).
[65] W. Del Pozzo, Phys. Rev. D **86**, 043011 (2012).
[66] B. S. Sathyaprakash, B. F. Schutz, and C. Van Den Broeck, Classical Quantum Gravity **27**, 215006 (2010).
[67] L. P. Singer, H.-Y. Chen, D. E. Holz, W. M. Farr, L. R. Price, V. Raymond, S. B. Cenko, N. Gehrels, J. Cannizzo, M. M. Kasliwal *et al.*, Astrophys. J. Lett. **829**, L15 (2016).
[68] C. Cutler and É. E. Flanagan, Phys. Rev. D **49**, 2658 (1994).
[69] M. Punturo, M. Abernathy, F. Acernese, B. Allen, N. Andersson, K. Arun, F. Barone, B. Barr, M. Barsuglia, M. Beker *et al.*, Classical Quantum Gravity **27**, 194002 (2010).
[70] B. P. Abbott, R. Abbott, T. D. Abbott, M. R. Abernathy, K. Ackley, C. Adams, P. Addesso, R. X. Adhikari, V. B. Adya, C. Affeldt *et al.*, Classical Quantum Gravity **34**, 044001 (2017).
[71] S. E. Dwyer, D. Sigg, S. Ballmer, L. Barsotti, N. Mavalvala, and M. Evans, Phys. Rev. D **91**, 082001 (2015).
[72] A. Loeb, Astrophys. J. Lett. **819**, L21 (2016).
[73] K. Murase, K. Kashiyama, P. Mészáros, I. Shoemaker, and N. Senno, Astrophys. J. Lett. **822**, L9 (2016).
[74] V. Connaughton, E. Burns, A. Goldstein, M. S. Briggs, B.-B. Zhang, C. M. Hui, P. Jenke, J. Racusin, C. A. Wilson-Hodge, P. N. Bhat *et al.*, Astrophys. J. Lett. **826**, L6 (2016).
[75] D. Jeong and F. Schmidt, Phys. Rev. D **86**, 083512 (2012).
[76] T. Namikawa, A. Nishizawa, and A. Taruya, Phys. Rev. D **94**, 024013 (2016).
[77] S. Vitale, W. Del Pozzo, T. G. F. Li, C. Van Den Broeck, I. Mandel, B. Aylott, and J. Veitch, Phys. Rev. D **85**, 064034 (2012).
[78] B. P. Abbott and LIGO Scientific Collaboration, arXiv:1602.03845.
[79] J. Veitch, I. Mandel, B. Aylott, B. Farr, V. Raymond, C. Rodriguez, M. van der Sluys, V. Kalogera, and A. Vecchio, Phys. Rev. D **85**, 104045 (2012).
[80] S. Fairhurst, Classical Quantum Gravity **28**, 105021 (2011).
[81] S. Vitale and M. Zanolin, Phys. Rev. D **84**, 104020 (2011).
[82] L. P. Singer and L. R. Price, Phys. Rev. D **93**, 024013 (2016).
[83] L. P. Singer, L. R. Price, B. Farr, A. L. Urban, C. Pankow, S. Vitale, J. Veitch, W. M. Farr, C. Hanna, K. Cannon *et al.*, Astrophys. J. **795**, 105 (2014).
[84] L. Singer (private communication).
[85] E. Baird, S. Fairhurst, M. Hannam, and P. Murphy, Phys. Rev. D **87**, 024035 (2013).
[86] T. A. Apostolatos, C. Cutler, G. J. Sussman, and K. S. Thorne, Phys. Rev. D **49**, 6274 (1994).
[87] B. Farr, E. Ochsner, W. M. Farr, and R. O'Shaughnessy, Phys. Rev. D **90**, 024018 (2014).
[88] A. Buonanno, Y. Chen, and M. Vallisneri, Phys. Rev. D **67**, 104025 (2003).
[89] A. Buonanno, Y. Chen, and M. Vallisneri, Phys. Rev. D **74**, 029904 (2006).
[90] M. Campanelli, C. O. Lousto, and Y. Zlochower, Phys. Rev. D **74**, 041501 (2006).
[91] C. M. Bishop, *Pattern Recognition and Machine Learning (Information Science and Statistics)* (Springer-Verlag, Secaucus, NJ, 2006).
[92] I. Mandel, W. M. Farr, A. Colonna, S. Stevenson, P. Tiňo, and J. Veitch, arXiv:1608.08223.